Supplementary Information

Photoinduced Vibrations Drive Ultrafast Structural Distortion in Lead Halide Perovskite

Hong-Guang Duan[1,2,3,*], Vandana Tiwari[1,4,*], Ajay Jha[1,*], Golibjon R. Berdiyorov[5], Alexey Akimov[6], Oriol Vendrell[7], Pabitra K. Nayak[8], Henry J. Snaith[8], Michael Thorwart[2,3], Zheng Li[9,1], Mohamed E. Madjet[5] & R. J. Dwayne Miller[1,3,10]

[1] *Max Planck Institute for the Structure and Dynamics of Matter, Luruper Chaussee 149, 22761, Hamburg, Germany*

[2] *I. Institut für Theoretische Physik, Universität Hamburg, Jungiusstraße 9, 20355 Hamburg, Germany*

[3] *The Hamburg Center for Ultrafast Imaging, Luruper Chaussee 149, 22761 Hamburg, Germany*

[4] *Department of Chemistry, University of Hamburg, Martin-Luther-King Platz 6, 20146 Hamburg, Germany*

[5] *Qatar Environment and Energy Research Institute, Hamad Bin Khalifa University, Qatar Foundation, P.O. Box 34110, Doha, Qatar*

[6] *Department of Chemistry, State University of New York at Buffalo, Buffalo NY, 14260, USA*

[7] *Physikalisch-Chemisches Institut, Universität Heidelberg, Im Neuenheimer Feld 229, 69120 Heidelberg, Germany*

[8] *Department of Physics, University of Oxford, Clarendon Laboratory, Parks Road, Oxford OX1 3PU, United Kingdom*

[9] *State Key Laboratory for Mesoscopic Physics, School of Physics, Peking University, Beijing 100871, China*

[10] *The Departments of Chemistry and Physics, University of Toronto, 80 St. George Street, Toronto Canada M5S 3H6*

(Dated: August 30, 2020)

In this Supplementary Information, we first describe the details of the correlation analysis and the global fitting approach. Second, we analyze the vibrational dynamics of the peaks related to the ground-state bleach (GSB) and the excited-state absorption (ESA) in the two-dimensional (2D) electronic spectrum. The details of the Tukey-window Fourier transform and wavelet analysis are described in the final section.

I. GLOBAL FITTING APPROACH

Multidimensional global fits of both experimental arrays of 2D spectra were performed in accordance with the available algorithm developed earlier [1]. A detailed description of the technique can be found in the Supplementary Information of Ref. [2]. In this method, a sequence of 2D spectra taken at different waiting times T are collected to form a three-dimensional array S(ω_τ, ω_t, T). This 3D array is then decomposed into a sum of two-dimensional decay-associated spectra $A_i(\omega_\tau, \omega_t)$ with individual exponential decays of correspondingly associated life times τ_i according to

$$\mathrm{S}(\omega_\tau, \omega_\mathrm{t}, \mathrm{T}) = \sum_\mathrm{i} \mathrm{A_i}(\omega_\tau, \omega_\mathrm{t}) \exp(-\mathrm{T}/\tau_\mathrm{i}). \tag{S1}$$

We apply the global fitting to the 2D electronic spectra of perovskite.

II. CORRELATION ANALYSIS IN 2D ELECTRONIC SPECTRA

To verify the origin of the oscillations observed in the 2D spectra, we have performed a cross-correlation analysis of the residuals across diagonal $\omega_\tau = \omega_t$. To quantify the correlation, we have calculated the correlation coefficients C between the residuals R for each pair of conjugated spectral positions in the delay time window up to 2 ps. The delay time steps were equally distributed with dt = 15 fs and the correlation coefficients are given by

$$\mathrm{C}(\omega_\mathrm{t}, \omega_\tau) = \mathrm{corr}(\mathrm{R}(\omega_\mathrm{t}, \omega_\tau, \mathrm{T}), \mathrm{R}(\omega_\tau, \omega_\mathrm{t}, \mathrm{T})), \tag{S2}$$

where corr evaluates the correlation with respect to T. This yields a 2D correlation spectrum.

III. TWO-DIMENSIONAL POWER SPECTRA OF VIBRATIONAL MODES AT 33 AND 48 CM^{-1}

In this section, we show the measured 2D power spectra of vibrational modes at 33 and 48 cm^{-1} in Fig. S1. They show the same features as the modes at 65 and 87 cm^{-1}, namely a strong magnitude located in the GSB and ESA regions. Moreover, these two areas are connected by a node in between, which indicates the opposite phase of the oscillations in the GSB and ESA regions. To identify the origin of these two modes, our theoretical calculations reveal that these two low-frequency modes are generated by the skeletal motion (I-Pb-I bending) of the sublattice in perovskite, which are presented in Fig. S2.

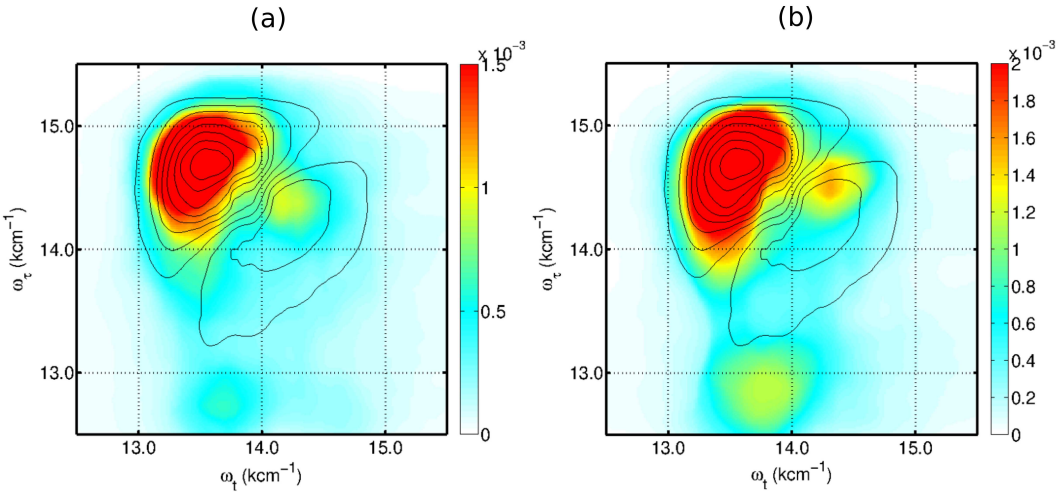

FIG. S1. Measured 2D power spectra of vibrational modes at 33 (a) and 48 (b) cm^{-1}. They show a strong amplitude in the GSB and ESA regions which are connected by a node.

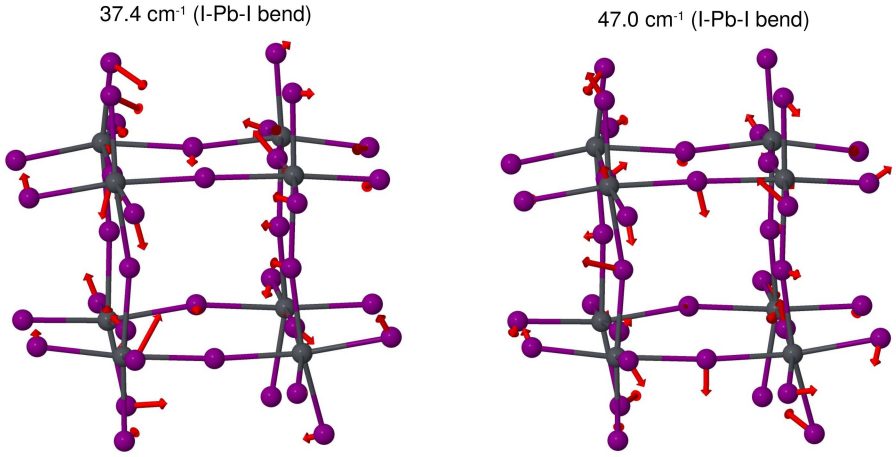

FIG. S2. The calculated vibrational modes at 37 and 47 cm^{-1}, respectively. Our theoretical calculations reveal that low-frequency vibrations originate from I-Pb-I bending motions of sublattice.

IV. VIBRATIONAL COHERENCES IN 2D ELECTRONIC SPECTROSCOPY

In this section, we examine the vibrational coherences of the GSB and ESA peaks in the 2D electronic spectra. For this, we first construct a model of a three-level system, in which the electronic ground state, the first and second excited states are denoted by $|g\rangle$, $|e_1\rangle$ and $|e_2\rangle$, respectively. We assign the optical transitions from $|g\rangle$ to $|e_1\rangle$ and from $|e_1\rangle$ to $|e_2\rangle$ to mimic the response signals of the GSB, stimulated emission and the ESA. Moreover, to study the coherent vibrational dynamics, the electronic ground and excited states are vibronically coupled to a vibrational mode. Here, we select an identified mode with a frequency of 180 cm^{-1}. By this, the system Hamiltonian is given as

$$H_S = |g\rangle\,\epsilon_g\,\langle g| + |e_1\rangle\,\epsilon_1\,\langle e_1| + |e_2\rangle\,\epsilon_2\,\langle e_2|\,, \tag{S3}$$

where ϵ_g, ϵ_1 and ϵ_2 are the site energies of the electronic ground, the first and second excited states, respectively. Moreover, a thermal reservoir of harmonic oscillators has been used to model the dissipative interactions with the environment. Thus, we have

$$\begin{aligned} H_{B_1} &= \sum_j \hbar\omega_j(\alpha_j^\dagger\alpha_j + 1/2), \\ H_{B_2} &= \sum_j \hbar\omega_j(\beta_j^\dagger\beta_j + 1/2), \end{aligned} \tag{S4}$$

where α_j ($\alpha_j^\dagger$) and β_j ($\beta_j^\dagger$) are the annihilation (creation) operators for the j-th bath mode with frequency of ω_j. For simplicity, we assume linear system-bath interactions, i.e.,

$$\begin{aligned} H_{SB_1} &= |e_1\rangle\,\langle e_1|\sum_j(c_j(\alpha_j^\dagger + \alpha_j)), \\ H_{SB_2} &= |e_2\rangle\,\langle e_2|\sum_j(d_j(\beta_j^\dagger + \beta_j)), \end{aligned} \tag{S5}$$

where, c_j and d_j are the coupling strengths of j-th mode to the electronic state. In addition, we assume the frequency distribution of bath to follow an Ohmic form with a Debye cutoff. Thus, the spectral density can be written as

$$J(\omega) = \frac{\hbar\eta_1}{\pi}\frac{\gamma_1^2\omega}{\gamma_1^2+\omega^2} + \frac{\hbar\eta_2}{\pi}\frac{4\gamma_2^2\omega_0^2\omega}{(\omega^2-\omega_0^2)+4\gamma_2^2\omega^2}, \tag{S6}$$

where $\eta_{1/2}$ and $\gamma_{1/2}$ are the coupling and damping constants, respectively. ω_0 is the frequency of a particular mode coupled to electronic states. To calculate this model, we assume $\epsilon_g = 0$, $\epsilon_1 = 800$ cm^{-1} and $\epsilon_2 = 2100$ cm^{-1}. In addition, we assume $\eta_1 = 1$, $\gamma_1 = 100$ cm^{-1}, $\eta_2 = 2.0$, $\gamma_2 = 20$ cm^{-1} and $\omega_0 = 500$ cm^{-1}. The transition diple is chosen as $\mu = |g\rangle\,\mu_{ge_1}\,\langle e_1| + |e_1\rangle\,\mu_{e_1e_2}\,\langle e_2|$. By this, we calculate the population dynamics and the 2D electronic spectra of this model using the hierarchy equation of motion [3, 4]. The details of this method and the way to calculate 2D electronic spectra have been described in Ref. [5]. We show the calculated 2D spectra in Fig. S3 for selected waiting times. In Fig. S3, we show that we are able to separate the ESA peak from the GSB peak completely by carefully selecting the site energies of ϵ_1 and ϵ_2. To examine the coherent dynamics, we extract the time-evolved amplitude of the GSB and ESA peaks, which are marked by "A" and "B" in Fig. S3 at T = 200 fs. We plot the traces of the GSB and ESA peaks as red and blue solid lines in Fig. S4. Moreover, we perform the global fitting on time series of the calculated 2D spectra. The fitted traces are shown in Fig. S4 as black dashed lines. The obtained residuals are shown in Fig. S6. In Fig. S6, we clearly observe the opposite phases of the oscillations in the residuals of the GSB and ESA peaks, respectively. By this, we demonstrate the anti-corrlated phases of the vibrational coherences of the optical signals from the GSB and ESA peaks in the 2D electronic spectra. Although it is based on a simple three-level model, we believe that this uncovered phase relation can be extended to the optical transitions between the valence and conduction bands in solid state dynamics.

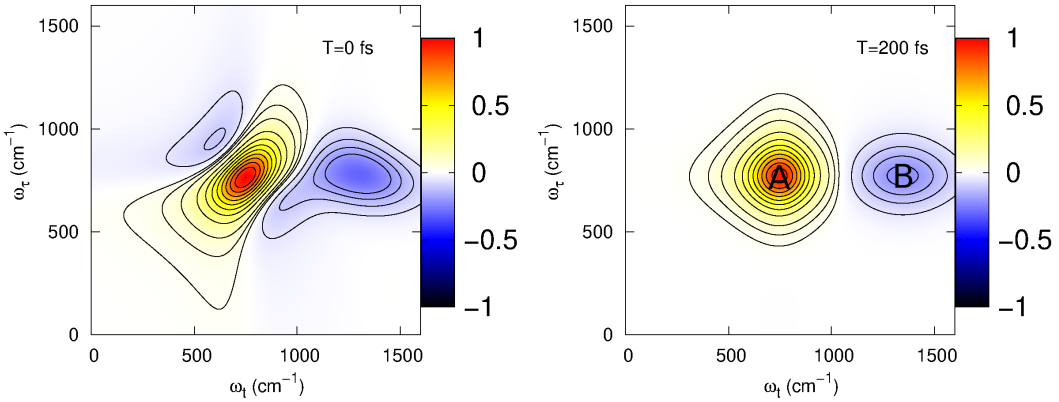

FIG. S3. Calculated 2D electronic spectra at T=0 (left) and 200 fs (right). The GSB and ESA peaks are marked by the positive and negative magnitudes in the 2D spectra.

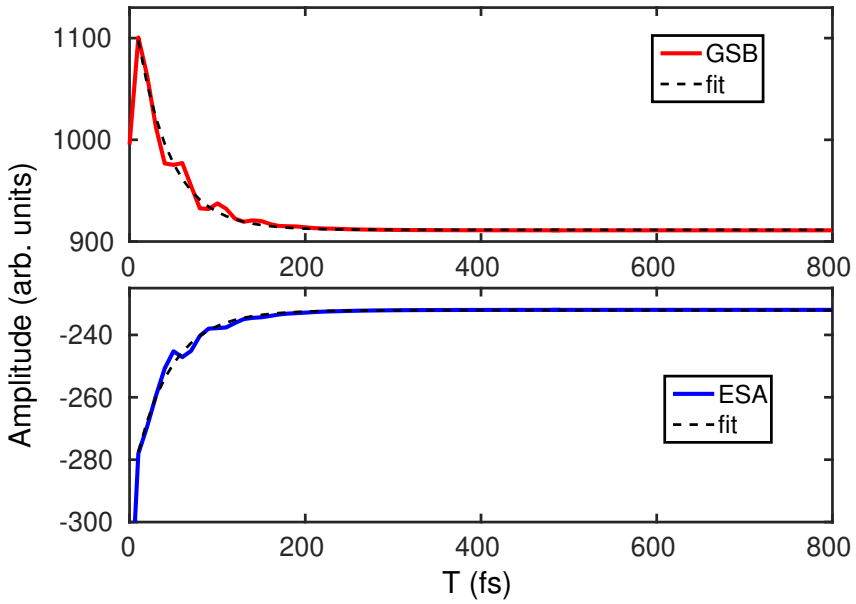

FIG. S4. The traces of the GSB (red solid line) and the ESA (blue solid line) from “A” and “B” in Fig. S3 at T=200 fs.

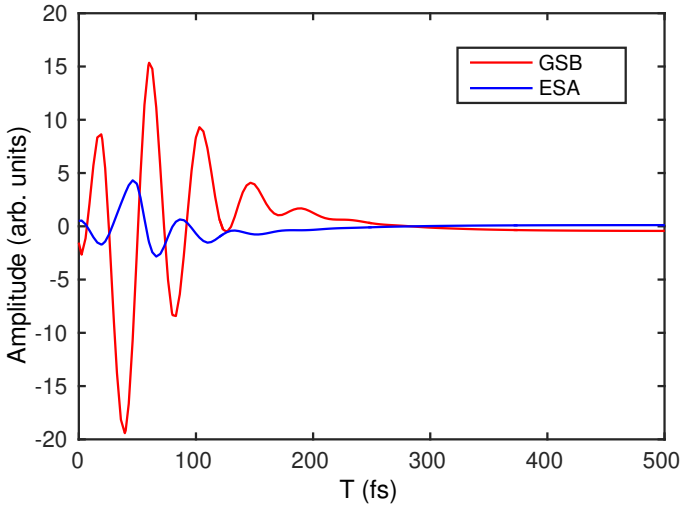

FIG. S5. Residuals of the GSB (red solid line) and the ESA (blue solid line) after removing the kinetics using a global fitting approach. They show opposite phases of oscillations of the GSB and ESA peaks.

V. TUKEY-WINDOW FOURIER TRANSFORM

Here, we provide the details related to the Fourier transform with the Tukey window. To isolate the high-frequency jitters, Fourier filtering in the frequency domain is employed. By this, we isolate each of these regions of interest with a Tukey window, which has the form

$$\omega(n) = \begin{cases} 1, & 0 \leq |n| \leq \alpha\frac{N}{2}\,, \\ \frac{1}{2}\left(1+\cos\left[\frac{\pi(n-\alpha\frac{N}{2})}{(1-\alpha)\frac{N}{2}}\right]\right), & \alpha\frac{N}{2} \leq |n| \leq \frac{N}{2}\,. \end{cases} \tag{S7}$$

Due to the flat top, it conserves the amplitudes of the Fourier components of interest over a larger frequency range than a cosine or a Gaussian window, while it still limits the artifacts arising from a pure bandpass filter. In this work, we use the Tukey window with $\alpha = 1/5$ and a Fourier bandpass filter with $\leq$700 cm^{-1}.

VI. RAW TRACES OF THE GSB AND ESA PEAKS

In this section, we show the raw data of the traces extracted from the GSB and ESA peaks. The high-frequency jitters are filtered by the Tukey-window Fourier transform.

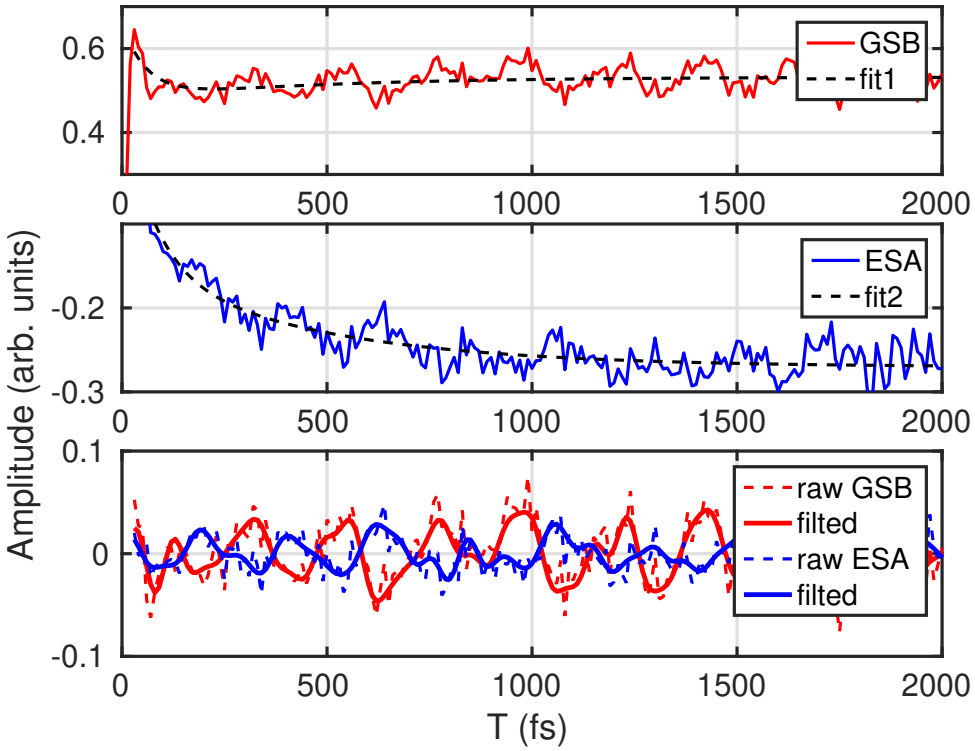

FIG. S6. Raw data of the trace from the GSB peak (red solid line). The kinetic fit is plotted as black dashed line. The raw data of the trace of the ESA peak is shown as blue solid line, the fitted trace is presented as black dashed line. The raw data and the polished residuals are shown as dashed and solid lines, respectively, in the lower panel.

VII. WAVELET ANALYSIS

In this section, we summarize the technical principles of the wavelet transform. The details are presented in Ref. [6, 7]. It starts from the definition of a zero mean and a short-time oscillating function ψ, called a "mother" wavelet, which is used to decompose a one- or multi-dimensional real-valued signal into different frequency bands. This mother wavelet function is translated in time by t and stretched by the scale of ω^{-1}, giving the wavelet "atom" function

$$\psi_{t,\omega}(t') = \sqrt{\omega}\psi([t'-t]\omega)\,. \tag{S8}$$

It provides the effective basis for the transformation. The two most common transforms are the discrete wavelet transform and the continuous wavelet transform [8]. The discrete one decomposes the signal into several frequency bands and is frequently used for data and image compression. The continuous one, which is used in this paper, is based on an expansion of a temporal signal $f(t)$ via the inner product of the function with a wavelet atom and reads

$$CWT_f(t,\omega) = \int_{-\infty}^{+\infty} dt' f(t')\sqrt{\omega}\psi^*([t'-t]\omega)\,. \tag{S9}$$

The parameter t indicates where the wavelet atom is centred, while the scale parameter ω^{-1} controls the relative width of the wavelet atom compared to the mother wavelet function. This nonlinear integral transform provides a high *time* resolution of high-frequency components, while for the slowly varying components of the signal, the *frequency* resolution is high. It projects the signal onto basis functions with a varying "center" frequency and a varying range fixed by the scaling factor.

VIII. TIME EVOLUTION OF ELECTRONIC CHARGE

In this section, we show the time evolution of electronic charge on the skeleton of perovskite in Fig. S7. After photoexcitation, the initial generated free carriers are mainly delocalized along Pb atoms in perovskite. This extra electronic charge on Pb atom enables the rotation of MA cation, which generates macroscopic signal of vibrational coherence of librational motion. The existed anharmonic interaction between MA cation and inorganic sublattice enable the coherent transfer of vibrational coherence from librational motion of MA cation to skeletal motion of perovskite. This coherent transfer enable perovskite to stabilize the electronic charge by enhancing particular coherence of skeletal motion. By this, the equilibrium state of electronic charge are reached by electron-phonon interaction at timescale of 700 fs. Moreover, we also show more detailed dynamics of vibrational coherences of perovskite in Fig. S8 after photoexcitation.

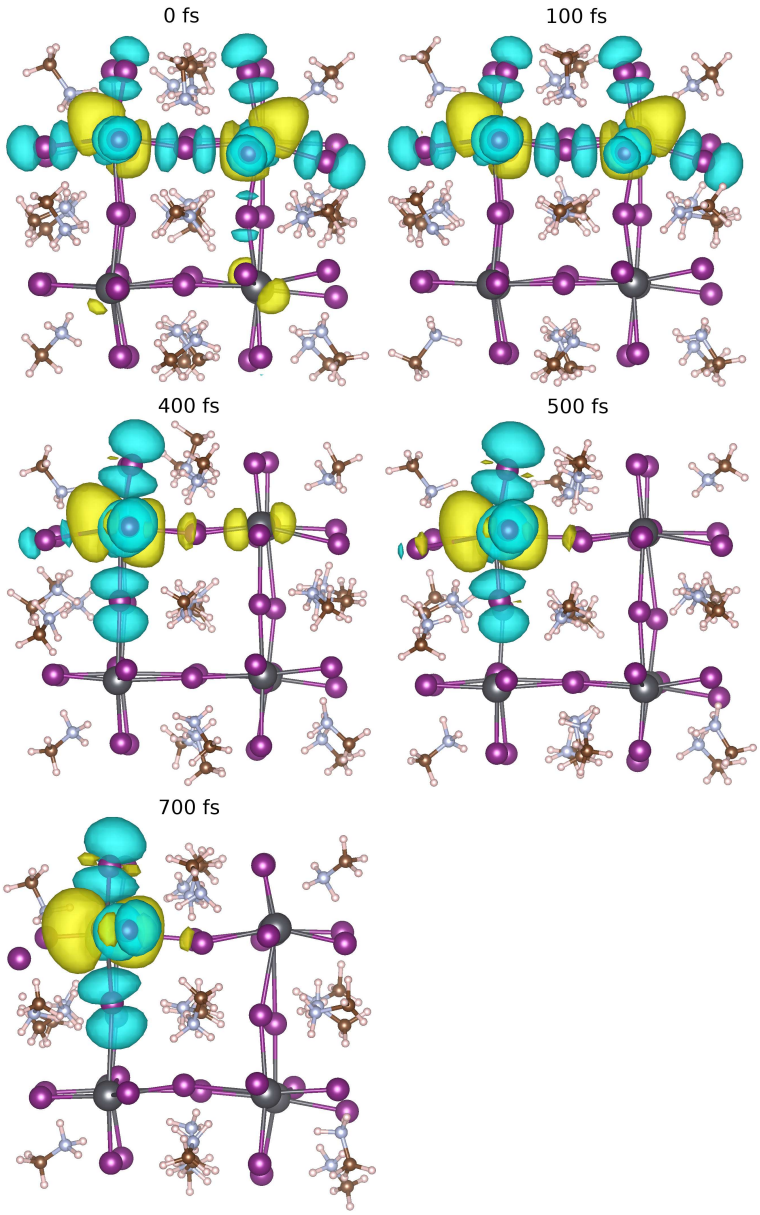

FIG. S7. Time evolution of electronic charge with the skeletal motion of perovskite. The free carriers are localized by electron-phonon interaction and the polaron formation at 700 fs.

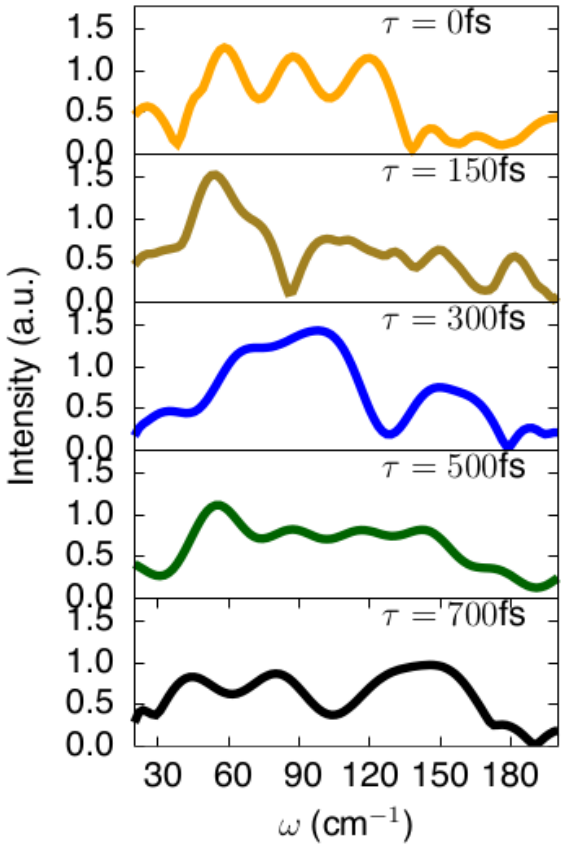

FIG. S8. Time-evolved vibrational coherences after photoexcitation.

IX. CHARGE LOCALISATION AT DIFFERENT CARRIER DENSITIES

In this section, we include excess electrons in our DFT simulations in order to model the excited state of the perovskite material as a first approximation. The considered value of the charge density (i.e., 10^{19} cm^{-3}) was chosen following the previous predictions. The main outcome of these calculations is that electrons are mainly localized on the Pb atoms (Fig. 4 (a)). We have also conducted electron localization function calculations for different values of the electron density. The results are shown in Fig. S9 for electron densities ranging from 10^{15} cm^{-3} to 5×10^{18} cm^{-3}. It is seen from this figure that regardless of the electron density, excess electrons are mainly localized near the Pb atoms. We would like to note that such electron injection method is used only in our static (i.e., electron localization function) calculations. Different method is used to perform the excited-state molecular-dynamics calculation which does not require such explicit charge injection.

We used the norm-conserving and relativistic pseudopotential PseudoDojo with medium basis set for all atoms with improved accuracy, which is implemented in the current version of the ATK software.

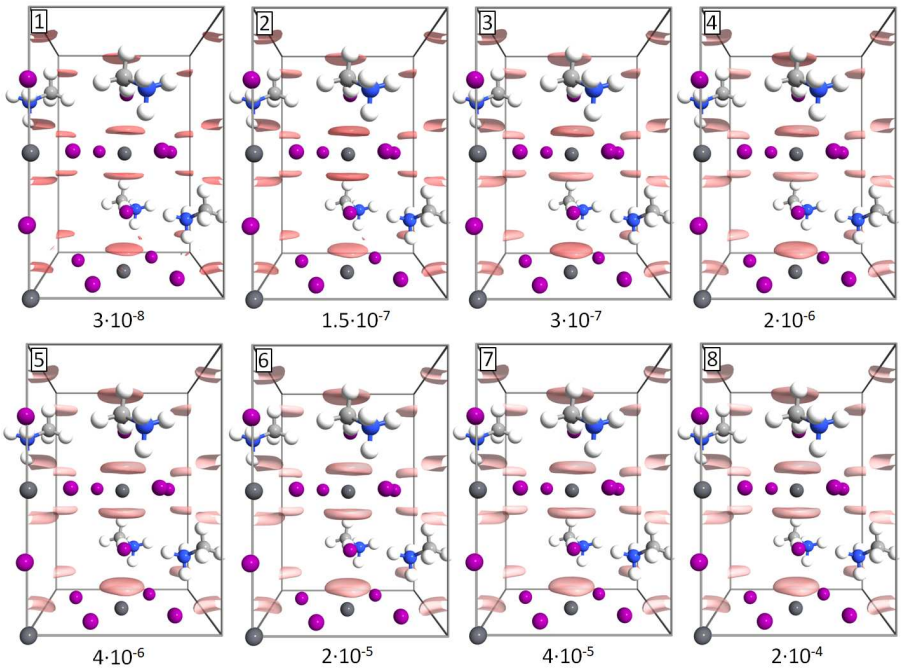

FIG. S9. Difference of electron localization functions with different level of excess electrons compared to its ground state: (1) $1 \times 10^{15} cm^{-3}$, (2) 5×10^{15} cm^{-3}, (3) 1×10^{16} cm^{-3}, (4) 5×10^{16} cm^{-3}, (5) 1×10^{17} cm^{-3}, (6) 5×10^{17} cm^{-3}, (7) 1×10^{18} cm^{-3} and (8) 5×10^{18} cm^{-3}. The number in each panel shows the isosurface value.

X. REFERENCES

[1] Prokhorenko, V. I. *European Photochemistry Association Newletter* June 2012, p21.

[2] Milota, F.; Prokhorenko, V. I.; Mancal, T.; Berlepsch, H. von; Bixner, O.; Kauffmann, H. F.; Hauer, J. Vibronic and Vibrational Coherences in Two-Dimensional Electronic Spectra of Supramolecular J-Aggregates. *J. Phys. Chem. A* **2013**, *117*, 6007-6014.

[3] Ishizaki, A.; Tanimura, Y. Quantum Dynamics of System Strongly Coupled to Low-temperature Colored Noise Bath: Reduced Hierarchy Equations Approach. *J. Phys. Soc. Jap.* **2005**, *74*, 3131-3134.

[4] Tanaka, M.; Tanimura, Y. Quantum Dissipative Dynamics of Electron Transfer Reaction System: Nonperturbative Hierarchy Equations Approach. *J. Phys. Soc. Jap.* **2009**, *78*, 073802.

[5] Duan, H. G.; Thorwart, M. Quantum Mechanical Wave Packet Dynamics at a Conical Intersection with Strong Vibrational Dissipation. *J. Phys. Chem. Lett.* **2016**, *7*, 382-386.

[6] Cohen, A.; Kovačevič, J. Wavelets: the Mathematical Background. *J. Proc. IEEE* **1996**, *84*, 514-522.

[7] Harrop, J. D.; Taraskin, S. N.; Elliot, S. R. Instantaneous Frequency and Amplitude Identification using Wavelets: Application to Glass Structure. *Phys. Rev. E* **2002**, *66*, 026703.

[8] van der Berg, J. *Wavelets in Physics* (Cambridge University Press, 2004).